

Oscillations and tidal deformations of crystallized white dwarfs

Yat-To Tang,¹* Lap-Ming Lin¹

¹*Department of Physics, The Chinese University of Hong Kong, Hong Kong, China*

Accepted XXX. Received YYY; in original form ZZZ

ABSTRACT

Long predicted more than fifty years ago, strong evidence for the existence of crystalline cores inside white dwarfs has recently been obtained by the Gaia space telescope. It is thus important to investigate how a crystalline core may affect the properties and dynamics of white dwarfs. In this paper, we first study the dependence of the frequencies of the fundamental (f), interfacial (i), and shear (s) oscillation modes on the size of the crystalline core. We find that the frequencies of the i- and s-modes depend sensitively on the size of the core, while the frequency of the f-mode is affected only slightly by at most a few percent for our chosen white dwarf models. We next consider the tidal deformability of crystallized white dwarfs and find that the effect of crystallization becomes significant only when the radius of the core is larger than about 70% of the stellar radius. The tidal deformability can change by a few to about 10 percent when a white dwarf becomes fully crystallized. We also show that there exist approximate equation-of-state insensitive relations connecting the mass, moment of inertia, tidal deformability, and f-mode frequency for pure fluid white dwarfs. Depending on the stellar mass and composition, however, these relations can be affected by a few percent when the white dwarf is crystallized. These changes could leave an imprint on the gravitational waves emitted from the late inspiral or merger of white dwarf binaries, which may be detectable by future space-borne gravitational wave detectors.

Key words: white dwarfs – stars: oscillations – gravitational waves

1 INTRODUCTION

White dwarfs (WDs) are among the most common stellar objects in the universe. It is estimated that our galaxy already hosts $\sim 10^8$ double white dwarf (DWD) binaries (Nelemans et al. 2001). Many of these binary systems are compact enough to be able to merge within the age of the universe. Furthermore, it is expected that gravitational wave (GW) signals emitted from DWD systems are detectable by future space-borne gravitational wave detectors, such as the Laser Interferometer Space Antenna (LISA, Amaro-Seoane et al. 2022), the Deci-hertz Interferometer Gravitational Wave Observatory (DECIGO, Kawamura et al. 2021), TianQin and Taiji (Ruan et al. 2020; Gong et al. 2021). Population synthesis models suggest that more than 10^4 DWDs could be resolved by LISA (Korol et al. 2017; Lamberts et al. 2019; Li et al. 2020; Breivik et al. 2020).

During the inspiral of a binary system, the oscillation modes of the stars may be excited, affecting the evolution of the system by transferring the orbital energy to the oscillation modes (Fuller & Lai 2011; Rathore et al. 2005) or even contributing directly to the GW emission. Although the effect on GW signal is small for DWD binaries, it is likely measurable by LISA for systems with high signal-to-noise ratio (Taylor et al. 2020). Furthermore, it is expected that DECIGO will detect 6600 DWD mergers per year (Kinugawa et al. 2022). The influence of mode excitation would be relevant for the GW signals emitted during the late inspiral and merger of these binaries. The oscillation modes of WDs have been widely investigated, focusing mostly on their gravity modes (see Córscico 2020, and references

therein). The tidal excitation of oscillation modes for binary WD systems has also been studied by Fuller & Lai (2011, 2012).

Meanwhile, the fundamental (f) mode frequency and tidal deformability of neutron stars are found to be connected by the f-Love relation (Chan et al. 2014), which is approximately equation-of-state (EOS) insensitive. The moment of inertia, tidal deformability, and rotational induced quadrupole moment of neutron stars are also connected by the I-Love-Q universal relations (Yagi & Yunes 2013a,b). These relations can be useful tools to infer the physical quantities of neutron stars. Furthermore, the I-Love-Q and f-Love relations have been used with the multiple Love relations (Yagi 2014) to reduce the intrinsic matter parameters in theoretical gravitational waveform models for binary neutron star inspirals that take into account the quadrupolar and octopolar adiabatic and dynamical tidal effects (Lackey et al. 2019; Schmidt & Hinderer 2019; Andersson & Pnigouras 2019; Barkett et al. 2020). The I-Love-Q relations have recently been extended to WDs (Boshkayev et al. 2017), though the relations are altered under differential rotation (Taylor et al. 2020) and could be broken for hot WDs (Boshkayev & Quevedo 2018). On the other hand, the f-Love relation has not been studied for WDs as far as we are aware. The universal relations for WDs are also relevant to the GW measurements of DWD binaries. By using the I-Love relation with another relation that connect the mass and moment of inertia of WDs, it has been proposed that the individual masses of a WD binary can be measured by considering the finite-size effects of the GW signal emitted by the system (Wolz et al. 2021).

Nevertheless, observable DWD binaries may have evolved long enough to be fully or partially crystallized. More than fifty years ago, van Horn (1968) has predicted the occurrence of crystallization

* E-mail: yttang@phy.cuhk.edu.hk

during WD cooling, suggesting that it may slow down the cooling process by the release of latent heat. Indirect evidence for the slow-down due to crystallization was observed for WDs in globular clusters (Winget et al. 2009; García-Berro et al. 2010; Campos et al. 2016). However, it is only recently that strong observational evidence for the existence of an isolated crystallization sequence of WDs in the Hertzsprung-Russell diagram has been obtained by the Gaia space telescope (Tremblay et al. 2019).

As the core crystallization of WDs is now well established, it is important to understand how it may affect the properties and dynamics of WDs. The oscillation modes of crystallized WDs have been studied mainly for the gravity mode (Montgomery & Winget 1999; Córscico et al. 2005; De Gerónimo et al. 2019; Althaus et al. 2021). Recently, Perot & Chamel (2022) have also shown that the tidal Love number of a crystallized WD can differ by a few percent comparing to its pure fluid counterpart. In this work, we shall first investigate how the core crystallization affects the f-mode, the interfacial (i) mode associated to the core-envelope interface, the shear (s) mode which is mainly confined in the solid core, and the tidal Love number for nonrotating WDs. We then establish the I-Love and f-Love relations for pure fluid WD models and examine how crystallization affects the validity of these relations.

The paper is organized as follows. In Section 2, we introduce the WD model used in this paper as well as the treatment of crystallization. In Section 3, we review the perturbation equations for determining the oscillation modes and tidal Love numbers. The numerical schemes for solving the perturbation equations are outlined in Section 4. The numerical results are presented in Section 5. Finally, we summarize and conclude our findings in Section 6. Throughout the paper, we assume geometric units with $G = c = 1$ unless otherwise specified.

2 STELLAR MODEL

We consider crystallized WD models consisting of a solid (inner) core and a surrounding fluid envelope. For the majority of the results presented in this study, the EOS given by Chamel & Fantina (2016) is adopted. The mass density ρ and pressure P are given by

$$\rho = \rho_N + \frac{m_e}{8\pi^2\lambda_e^3} \left[x_r (1 + 2x_r^2) \sqrt{1 + x_r^2} - \ln \left(x_r + \sqrt{1 + x_r^2} \right) \right] \times \left(1 + \frac{\alpha}{2\pi} \right) - n_e m_e + C_M \left(\frac{4\pi}{3} \right)^{1/3} \frac{e^2}{c^2} n_e^{4/3} Z_{\text{eff}}^{2/3}, \quad (1)$$

$$P = \frac{m_e c^2}{8\pi^2\lambda_e^3} \left[x_r \left(\frac{2}{3} x_r^2 - 1 \right) \sqrt{1 + x_r^2} + \ln \left(x_r + \sqrt{1 + x_r^2} \right) \right] \times \left(1 + \frac{\alpha}{2\pi} \right) + \frac{C_M}{3} \left(\frac{4\pi}{3} \right)^{1/3} e^2 n_e^{4/3} Z_{\text{eff}}^{2/3}, \quad (2)$$

where ρ_N is the mass density of the nuclei, m_e is the mass of electron, n_e is the number density of electron, $C_M = -0.895929255682$ is the Madelung constant (Baiko et al. 2001), α is the fine structure constant, e is the elementary charge, c is the speed of light, $x_r = \lambda_e k_e$ is a dimensionless relativity parameter with λ_e being the electron Compton wavelength and k_e being the electron Fermi wave number; $Z_{\text{eff}} = Z\sigma(Z)^{3/2}$ is the effective nuclear charge for nuclei with atomic number Z , where

$$\sigma(Z) = 1 + \alpha \frac{12^{4/3}}{35\pi^{1/3}} \left(1 - 1.1866Z^{-0.267} + 0.27Z^{-1} \right) Z^{2/3}. \quad (3)$$

The EOS corresponds to a zero-temperature Coulomb plasma with atomic nuclei of single species. The hydrogen, helium layers and the

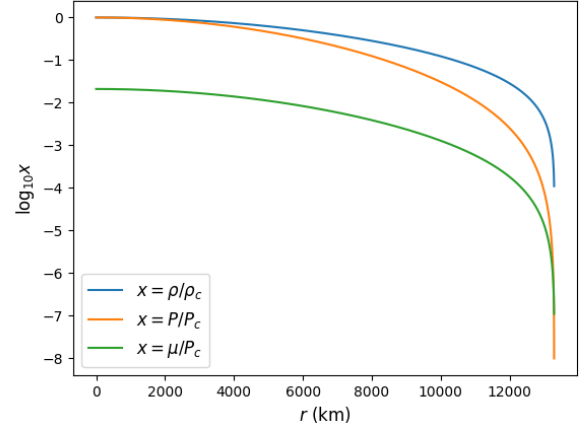


Figure 1. The profiles of density ρ , pressure P , and shear modulus μ for a $0.20M_{\odot}$ WD model made of ^{16}O . The density and pressure are normalized by their central values, while the shear modulus is normalized by the central pressure.

atmosphere are ignored as they contribute not more than $\sim 1\%$ of the total mass (Saumon et al. 2022). The type of nuclei in the core of WD may be carbon, oxygen, helium (Nelemans & Tauris 1998; Liebert et al. 2004; Benvenuto & De Vito 2005), neon, magnesium (Nomoto 1984), or even iron (Isern et al. 1991; Jordan et al. 2012). The EOS is effectively the Chandrasekhar model (Chandrasekhar 1931, 1935, 1939) with extra effects implemented, including the lattice, electron exchange, and screening corrections. Besides considering this EOS model with different atomic nuclei, we shall also consider the BPS EOS (Baym et al. 1971) and the original Chandrasekhar EOS (Chandrasekhar 1931, 1935, 1939) when we examine the sensitivity of universal relations with respect to different EOS models. Although the BPS model is not a realistic model for white dwarfs, the inclusion of it can test for the robustness of universal relations.

Assuming the solid core to be isotropic, the elastic properties of the core are described by the effective shear modulus (Chugunov 2021)

$$\mu = 0.119457234091 \left(\frac{4\pi}{3} \right)^{1/3} Z^{2/3} e^2 n_e^{4/3}. \quad (4)$$

Note that this expression only gives an upper limit of μ as it is obtained from a Voigt average (Kobyakov & Pethick 2015).

The nonrotating background stellar model is obtained by integrating the hydrostatic equilibrium equations in Newtonian gravity

$$\frac{dm}{dr} = 4\pi\rho r^2, \quad (5)$$

$$\frac{dP}{dr} = -\rho g, \quad (6)$$

where $m(r)$ is the mass enclosed inside the radial coordinate r and $g = m/r^2$ is the local gravitational acceleration. The system is closed by a given EOS model $P(\rho)$. As an illustration of a typical WD model in our study, we plot the profiles of ρ , P , and μ for a $0.20M_{\odot}$ WD made of ^{16}O in Figure 1.

3 PERTURBATION EQUATIONS

In this section, we review the perturbation equations which are solved to obtain the oscillation modes and tidal Love number of our crystallized WD models. The motion of a mass element is governed by the mass conservation equation, momentum equation, and Poisson equation:

$$\partial_t \rho + \partial_i(\rho v_i) = 0, \quad (7)$$

$$\partial_t v_i + v_j \partial_j v_i = \frac{1}{\rho} \partial_j \sigma_{ij} - \partial_i \Phi, \quad (8)$$

$$\partial_i \partial_i \Phi = 4\pi \rho, \quad (9)$$

where the Latin indices (i, j) refer to the spatial coordinates, ρ is the mass density, v_i is the velocity of a mass element, σ_{ij} is the stress tensor, and Φ is the gravitational potential. To study the oscillation modes of a given background stellar model, the above equations are perturbed by assuming $q = q_0 + \delta q$ and keeping only terms of first order in δq , where q denotes any physical variable such as ρ and q_0 is its value evaluated on the unperturbed background model. Hereafter δq is used to represent the Eulerian perturbation of q and Δq is the Lagrangian perturbation.

We assume the unperturbed background star to be in hydrostatic equilibrium without rotation, and hence $\vec{v}_0 = 0$ and $\delta v_i = \partial_t u_i$, where u_i is the Lagrangian displacement. The equilibrium background is also assumed to be an inviscid fluid under zero strain, and the stress is only given by the isotropic pressure, i.e. $\sigma_{0,ij} = -P_0 \delta_{ij}$, where δ_{ij} is the Kronecker delta. For the treatment of elasticity, any nonzero strain is produced by the change of stress at the perturbative level. Assuming adiabatic motion for the isotropic elastic solid core, the Lagrangian perturbation of the stress tensor is given by

$$\Delta \sigma_{ij} = (\Gamma_1 P_0 u_{kk}) \delta_{ij} + 2\mu(u_{ij} - \frac{1}{3} u_{kk} \delta_{ij}), \quad (10)$$

where $\Gamma_1 = d \ln P_0 / d \ln \rho_0$, μ is the shear modulus, and u_{ij} is the strain tensor, defined by $u_{ij} = \frac{1}{2}(\partial_j u_i + \partial_i u_j)$. As a result, the set of perturbed dynamical equations can be written as

$$\delta \rho + \partial_i(\rho u_i) = 0, \quad (11)$$

$$\rho \partial_t^2 u_i = \partial_j \delta \sigma_{ij} - \rho \partial_i \delta \Phi - \delta \rho \partial_i \Phi, \quad (12)$$

$$\partial_i \partial_i \delta \Phi = 4\pi \delta \rho, \quad (13)$$

where

$$\begin{aligned} \partial_j \delta \sigma_{ij} = & \partial_i(\Gamma_1 P \partial_j u_j) + \partial_i(u_j \partial_j P) - \partial_i \left(\frac{2}{3} \mu \partial_j u_j \right) + (\partial_j \mu \partial_j) u_i \\ & + \partial_i(u_j \partial_j \mu) - (u_j \partial_j) \partial_i \mu + \mu(\partial_j \partial_j u_i + \partial_i \partial_j u_j). \end{aligned} \quad (14)$$

Note that hereafter the subscript 0 is dropped for unperturbed background quantities.

By combining the perturbed dynamical equations and taking an oscillatory time dependence for all perturbed scalar quantities $\delta q(x_i, t) = \delta \bar{q}(x_i) \exp(i\omega t)$ and the Lagrangian displacement $u_i(x_i, t) = \xi_i(x_i) \exp(i\omega t)$, where ω is the oscillation frequency, one can derive the linear adiabatic wave equation for non-radial oscillations. The angular dependence can be further separated by expanding the perturbed variables in terms of spherical harmonics $Y_{lm}(\theta, \phi)$. In this study, we shall only consider the class of spheroidal modes

for which ξ_i and $\delta \bar{q}$ are expanded according to

$$\xi_r(r, \theta, \phi) = U(r) Y_{lm}(\theta, \phi), \quad (15)$$

$$\xi_\theta(r, \theta, \phi) = V(r) \frac{\partial Y_{lm}(\theta, \phi)}{\partial \theta}, \quad (16)$$

$$\xi_\phi(r, \theta, \phi) = \frac{V(r)}{\sin \theta} \frac{\partial Y_{lm}(\theta, \phi)}{\partial \phi}, \quad (17)$$

$$\delta \bar{q}(r, \theta, \phi) = \delta \bar{q}(r) Y_{lm}(\theta, \phi). \quad (18)$$

Making use of the above expansions, the linear adiabatic wave equation can be recast into a set of differential equations. Let us introduce the variables defined in [Alterman et al. \(1959\)](#) and [Crossley \(1975\)](#):

$$y_1 = U, \quad (19)$$

$$y_2 = \lambda X + 2\mu \frac{dU}{dr}, \quad (20)$$

$$y_3 = V, \quad (21)$$

$$y_4 = \mu \left(\frac{dV}{dr} - \frac{V}{r} + \frac{U}{r} \right), \quad (22)$$

$$y_5 = -\delta \bar{\Phi}, \quad (23)$$

$$y_6 = -\frac{d\delta \bar{\Phi}}{dr} - 4\pi \rho U, \quad (24)$$

where $X = \frac{1}{r^2} \frac{d}{dr}(r^2 U) - \frac{l(l+1)}{r} V$; $\lambda = \Gamma_1 P - \frac{2}{3}\mu$; y_1 and y_3 are the radial and transverse displacements, respectively; y_2 and y_4 are the radial and transverse tractions; y_5 and y_6 are related to the perturbation of gravitational potential and its derivative. The differential equations then read ([Alterman et al. 1959](#); [Crossley 1975](#))

$$y_1' = -\frac{2\lambda\beta}{r} y_1 + \beta y_2 + \frac{l(l+1)\lambda\beta}{r} y_3, \quad (25)$$

$$\begin{aligned} y_2' = & \left[-\rho\omega^2 - \frac{4\rho g}{r} + \frac{2\delta}{r^2} \right] y_1 - \frac{4\mu\beta}{r} y_2 + l(l+1) \left[\frac{\rho g}{r} - \frac{\delta}{r^2} \right] y_3 \\ & + \frac{l(l+1)}{r} y_4 - \rho y_6, \end{aligned} \quad (26)$$

$$y_3' = -\frac{1}{r} y_1 + \frac{1}{r} y_3 + \frac{1}{\mu} y_4, \quad (27)$$

$$y_4' = \left[\frac{\rho g}{r} - \frac{\delta}{r^2} \right] y_1 - \frac{\lambda\beta}{r} y_2 + \left[-\rho\omega^2 + \frac{\epsilon}{r^2} \right] y_3 - \frac{3}{r} y_4 - \frac{\rho}{r} y_5, \quad (28)$$

$$y_5' = 3\gamma y_1 + y_6, \quad (29)$$

$$y_6' = -3\gamma \frac{l(l+1)}{r} y_3 + \frac{l(l+1)}{r^2} y_5 - \frac{2}{r} y_6, \quad (30)$$

where $\beta = (\lambda + 2\mu)^{-1}$, $\gamma = \frac{4}{3}\pi\rho$, $\delta = 2\mu(3\lambda + 2\mu)\beta$, and $\epsilon = 4l(l+1)\mu(\lambda + \mu)\beta - 2\mu$. Note that in [Crossley \(1975\)](#), the last term in equation (26) is $-\frac{\rho}{r} y_6$, which is a typo.

In the fluid envelope where $\mu = 0$, we have $\beta = \lambda^{-1}$, $\delta = \epsilon = 0$, $\lambda = \Gamma_1 P$, and $y_4 = 0$. Therefore, the six differential equations (25)-(30) reduce to ([Alterman et al. 1959](#))

$$y_1' = -\frac{2}{r} y_1 + \frac{1}{\lambda} y_2 + \frac{l(l+1)}{r} y_3, \quad (31)$$

$$y_2' = -(\rho\omega^2 + \frac{4\rho g}{r}) y_1 + \frac{l(l+1)\rho g}{r} y_3 - \rho y_6, \quad (32)$$

$$y_5' = 4\pi\rho y_1 + y_6, \quad (33)$$

$$y_6' = -\frac{4\pi\rho l(l+1)}{r} y_3 + \frac{l(l+1)}{r^2} y_5 - \frac{2}{r} y_6, \quad (34)$$

where

$$\rho\omega^2 y_3 = \frac{\rho g}{r} y_1 - \frac{1}{r} y_2 - \frac{\rho}{r} y_5. \quad (35)$$

This is equivalent to the standard four differential equations (see, e.g., [Cox 1980](#)) for a pure fluid star.

To solve the differential equations, one must specify the boundary conditions (BCs) at the center, core-envelope interface, and surface. The central BC is obtained by requiring the variables to be regular at the center (see [Crossley 1975](#)):

$$y_1 = Ar^{l-1} + A'r^{l+1}, \quad (36)$$

$$y_2 = Br^{l-2} + B'r^l, \quad (37)$$

$$y_3 = Cr^{l-1} + C'r^{l+1}, \quad (38)$$

$$y_4 = Dr^{l-2} + D'r^l, \quad (39)$$

$$y_5 = Er^l + E'r^{l+2}, \quad (40)$$

$$y_6 = Fr^{l-1} + F'r^{l+1}, \quad (41)$$

where the coefficients A, B, C , etc, are given by

$$A = IC, \quad (42)$$

$$B = 2l(l-1)\mu C, \quad (43)$$

$$D = 2(l-1)\mu C, \quad (44)$$

$$E = 3\gamma C + \frac{F}{l}, \quad (45)$$

and

$$C' = \frac{p_2}{p_1}D' + \frac{\rho}{p_1}\{F + [\omega^2 + (3-l)\gamma]A\}, \quad (46)$$

$$B' = -q_1C' + q_2D', \quad (47)$$

$$A' = -lC' + \frac{1}{\mu}D', \quad (48)$$

$$E' = \frac{3\gamma}{2(2l+3)}[(l+3)A' - l(l+1)C'], \quad (49)$$

$$F' = (l+2)E' - 3\gamma A', \quad (50)$$

with

$$p_1 = 2l^2(l+2)\lambda + 2l(l^2 + 2l - 1)\mu, \quad (51)$$

$$p_2 = l(l+5) + l(l+3)\frac{\lambda}{\mu}, \quad (52)$$

$$q_1 = 2l(l+2)\lambda + 2l(l+1)\mu, \quad (53)$$

$$q_2 = 2(l+1) + (l+3)\frac{\lambda}{\mu}. \quad (54)$$

The above expansions are used in equations (25)-(30) to start the integration near the center. However, severe numerical cancellation occurs for y_2', y_4' , and y_6' when $l \geq 1$. To fix the problem, we need to expand y_2', y_4' and y_6' as well. More details about the BCs are presented in Appendix A.

At the core-envelope interface, the traction, radial displacement, gravitational potential, and its derivative are continuous, thus one requires all the independent variables (except y_3) to be continuous ([Alterman et al. 1959](#)). The BCs at the stellar surface are $y_2 = 0$, which can be obtained from the vanishing of the Lagrangian perturbation of the pressure, and the continuity of the gravitational potential and its derivative

$$y_6 + \frac{l+1}{r}y_5 = 0. \quad (55)$$

4 NUMERICAL SCHEME

4.1 Oscillations

For the central BC, there are 3 independent variables (C, F, D'). We choose three orthogonal sets of them, such as

$(1, 0, 0), (0, 1, 0), (0, 0, 1)$. After integrating the differential equations, we obtain 3 independent solutions in the solid core, denoted as $\vec{Y}_1(r), \vec{Y}_2(r)$ and $\vec{Y}_3(r)$, where the components of the abstract vectors \vec{Y}_i are $(y_1, y_2, y_3, y_4, y_5, y_6)$. Similarly, we obtain 2 independent solutions $\vec{Y}_4(r)$ and $\vec{Y}_5(r)$ by integrating the differential equations from the surface to the interface in the fluid envelope. The interfacial BC gives the relation between these solutions, namely

$$w_1\vec{Y}_1(R_c) + w_2\vec{Y}_2(R_c) + w_3\vec{Y}_3(R_c) = w_4\vec{Y}_4(R_c) + w_5\vec{Y}_5(R_c), \quad (56)$$

for all the components except y_3 , where the w 's are some real constants, and R_c is the radius of the core. This equation is due to the continuity of the y 's (except y_3). The last coefficient w_5 only accounts for an arbitrary normalization and can be set to 1.

The above equation can be rewritten as a matrix equation

$$\begin{pmatrix} Y_{1,1} & Y_{2,1} & Y_{3,1} & Y_{4,1} \\ Y_{1,2} & Y_{2,2} & Y_{3,2} & Y_{4,2} \\ Y_{1,4} & Y_{2,4} & Y_{3,4} & Y_{4,4} \\ Y_{1,5} & Y_{2,5} & Y_{3,5} & Y_{4,5} \end{pmatrix} \begin{pmatrix} w_1 \\ w_2 \\ w_3 \\ -w_4 \end{pmatrix} = \begin{pmatrix} Y_{5,1} \\ Y_{5,2} \\ Y_{5,4} \\ Y_{5,5} \end{pmatrix}, \quad (57)$$

together with an algebraic equation

$$w_1Y_{1,6} + w_2Y_{2,6} + w_3Y_{3,6} = w_4Y_{4,6} + Y_{5,6}, \quad (58)$$

where $Y_{i,j}$ is the j -th component of $Y_i(R_c)$ and we have set $w_5 = 1$. For a given ω , equation (57) determines the coefficients w_i , and the value of ω is a normal mode frequency if equation (58) is satisfied. We scan through a range of ω to search for the normal modes.

4.2 Tidal Love number and deformability

For the static tide limit we consider in this work, the tidal Love number can be computed using the same set of perturbation equations in Section 3 by setting $\omega = 0$. This time, the surface boundary condition is replaced by a matching with the exterior solution, thus we integrate from the center up to the surface, in contrast to integrating separately from the center and the surface to the interface, as discussed in Section 4.1.

At the center, we again choose 3 orthogonal sets of initial conditions, and obtain 3 independent solutions $\vec{Y}_1(r), \vec{Y}_2(r)$, and $\vec{Y}_3(r)$ by integrating from the center to the core-envelope interface. By setting $\omega = 0$, we have

$$y_2 - \rho g y_1 + \rho y_5 = 0 \quad (59)$$

in the fluid envelope, and $y_4 = 0$ at the interface. The first equation comes from equation (35), while the second is simply the interfacial boundary condition. These two conditions are enough to determine the solution.

As the general solution is a linear combination of all 3 independent solutions, the above 2 equations can be rewritten as

$$w_1A_1(R_c) + w_2A_2(R_c) + w_3A_3(R_c) = 0 \quad (60)$$

$$w_1Y_{1,4}(R_c) + w_2Y_{2,4}(R_c) + w_3Y_{3,4}(R_c) = 0, \quad (61)$$

where $A_i(r) = Y_{i,2}(r) - \rho g Y_{i,1}(r) + \rho Y_{i,5}(r)$, and the w 's are some real constants. The last coefficient w_3 is again set to 1. From equations (60) and (61), w_1 and w_2 are determined, thus the solution at the interface is known, and we can continue integrating towards the surface.

In the fluid envelope with $\omega = 0$, it can be shown that equations (31)-(35) can be combined and reduced to the standard second-order differential equation for determining the tidal Love number in

Newtonian gravity (e.g., Yagi & Yunes 2013a; Chan et al. 2014)

$$\frac{1}{r^2} \frac{d}{dr} \left(r^2 \frac{dH}{dr} \right) - \frac{l(l+1)}{r^2} H = -4\pi \left(\frac{1}{\rho} \frac{dP}{d\rho} \right)^{-1} H, \quad (62)$$

where $H \equiv \delta\tilde{\Phi}$. At the surface, we can define a quantity $\eta = rH'(R)/H(R)$, where $H(R)$ is obtained by integrating the above equation and evaluated at the star surface, and $H'(R)$ is its derivative. By matching the interior solution at the surface with the exterior perturbed potential (see, e.g., Poisson & Will (2014)), the Love number k_l is determined by

$$k_l = \frac{l - \eta}{2(\eta + l + 1)}. \quad (63)$$

In the discussion of the f-Love relation (Chan et al. 2014), we shall focus on the dimensionless quantity $\bar{\lambda}_l \equiv \lambda_l/M^{2l+1}$, where the tidal deformability λ_l is related to k_l by

$$\lambda_l = \frac{2}{(2l-1)!!} k_l R^{2l+1}, \quad (64)$$

where M and R are the total mass and radius of the star, respectively.

5 RESULTS

In the following, we present our numerical results on oscillations in Section 5.1, tidal deformability in Section 5.2, and universal relations in Section 5.3. We focus on quadrupolar perturbations so that $l = 2$ is assumed for the perturbation equations presented in Section 3. The subscript l in the tidal deformability is thus omitted.

5.1 Oscillation modes

We first discuss the effect of crystallization on the oscillation modes, including the fundamental mode (f-mode), shear mode (s-mode), and interfacial mode (i-mode). The f-mode can be regarded as the fundamental pressure mode with no radial nodes. Unlike the f-mode, the s-mode and i-mode do not appear in pure fluid stellar models. The former is restored by the elastic stresses in the solid core, and the latter is due to the core-envelope interface. As we assume no composition gradient, there is no gravity mode. Higher-order pressure modes are not considered as well.

The change of pressure mode frequency due to elasticity can be estimated by the μ/P ratio (Montgomery & Winget 1999), which is about a few percent as shown in Figure 1. Therefore, it is expected that the f-mode will also be shifted by a few percent due to crystallization. Moreover, in Figure 1, one can see that the ratio μ/P is higher at lower density. We found that throughout the density range relevant for WDs, the ratio increases as the density decreases, thus it is expected that the f-mode frequency will show a larger change for stars with lower mass.

In Figure 2, the frequency spectrum of a $0.20M_{\odot}$ ^{16}O star is shown as a function of the solid core radius R_c (normalized by the stellar radius R), which is treated as a free parameter in our study. When there is no solid core (i.e., $R_c = 0$), the s- and i-modes do not exist, and the f-mode is represented by the blue data points in the figure. As the core radius increases, the frequency of the f-mode essentially remains unchanged, while the frequency of the i-mode (green data) decreases toward the f-mode. At $R_c/R = 0.15$, there is an avoid crossing between the f-mode and i-mode. When R_c increases further, the i-mode keeps decreasing as shown by the lower branch of the green line after the avoid-crossing point. The f-mode remains nearly unchanged (blue line) until another avoid crossing occurs at

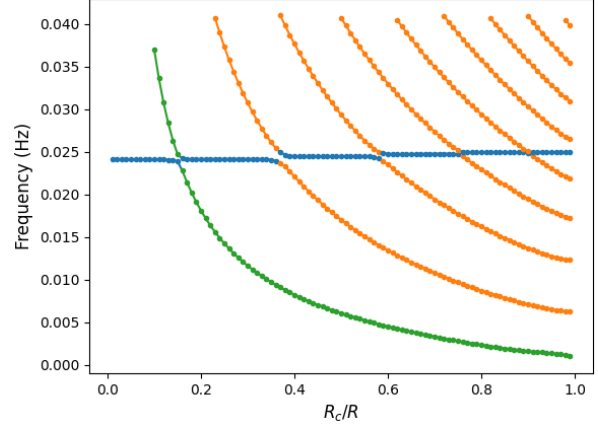


Figure 2. The frequency spectrum of a crystallized $0.20M_{\odot}$ ^{16}O star is plotted as a function of the (normalized) core radius. The f-mode, i-mode, and s-modes are denoted by the blue line, green line, and orange lines respectively. Avoided crossing occurs when any two modes are about to "cross" each other.

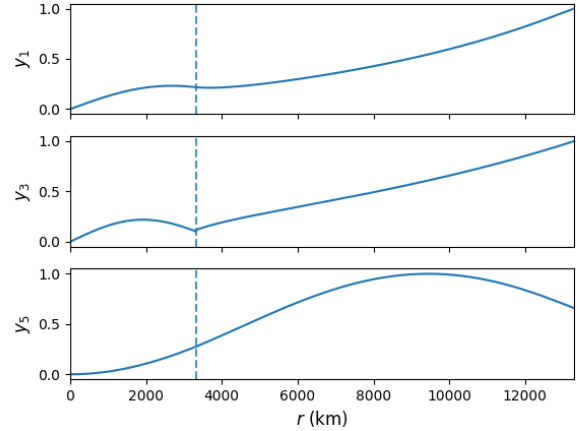


Figure 3. Eigenfunctions for the f-mode of a $0.20M_{\odot}$ ^{16}O star with crystallized core radius $R_c = 0.25R$, normalized by their maximum amplitudes. The core-envelope interface is denoted by the dashed line.

$R_c/R = 0.37$ between the f-mode and the fundamental s-mode (s_1), which is represented by the first branch of orange data points after the green line. A few other avoided crossings between the f-mode and higher order s-modes are observed as R_c/R approaches 1. Near an avoided crossing, the modes exchange characteristics with each other, and their frequencies deviate from the values they would have if there is no avoided crossing. The deviation is most significant at the crossing between the f and s_1 mode. Furthermore, as R_c/R increases from 0 to 1, the f-mode frequency increases in steps at each avoided crossing. The step is larger at lower R_c/R , but as R_c/R approaches 1, the step becomes very small. At $R_c/R = 1$, however, the i-mode no longer exists, and hence we only show the mode frequencies up to $R_c/R = 0.99$.

Next, we show the eigenfunctions y_1 , y_3 , and y_5 for different oscillation modes. Let us recall that y_1 and y_3 are the radial and transverse displacements, respectively; y_5 is related to the poten-

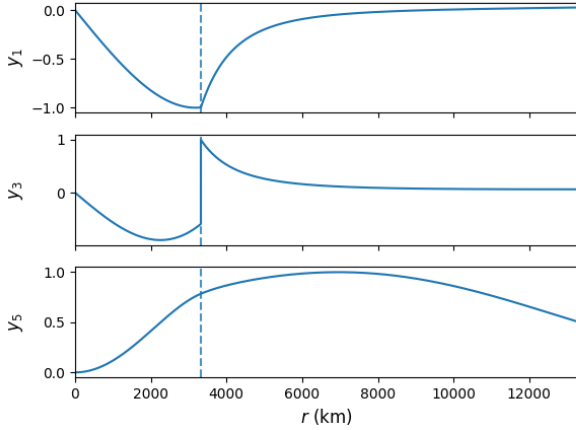


Figure 4. Similar to Figure 3, but for the i-mode.

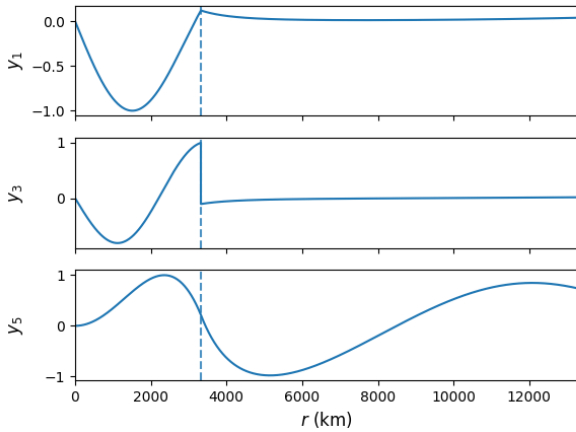


Figure 5. Similar to Figure 3, but for the s_1 -mode.

tial perturbation. In Figures 3, 4, and 5, the eigenfunctions of the f-mode, i-mode, and s_1 -mode are presented respectively. All of them are computed for a $0.20M_{\odot}$ ^{16}O WD model with $R_c/R = 0.25$, and normalized by their own maximum amplitudes. In each figure, the vertical dashed line represents the position of the core-envelope interface. The characteristic of f-mode is the overall increasing trend of the fluid displacements (y_1 and y_3). In particular, the fluid displacements increase monotonically toward the star surface in the fluid envelope just like the behavior for a pure fluid star. Inside the solid core, the displacements may be oscillating, but the overall increasing trend remains. The discontinuity in the transverse displacement (y_3) is also small for the f-mode. On the other hand, the i-mode is characterized by the large displacements at the interface, as well as the large discontinuity in the transverse displacement. The potential perturbation y_5 for the i-mode is continuous across the core-envelope interface as it should be.

For the s_1 -mode in Figure 5, the main feature is the strong oscillations in the solid core. The order of the s-mode in general can be told by the number of nodes in the displacements in the solid core. For instance, the s_1 mode has one node in both y_1 and y_3 in the

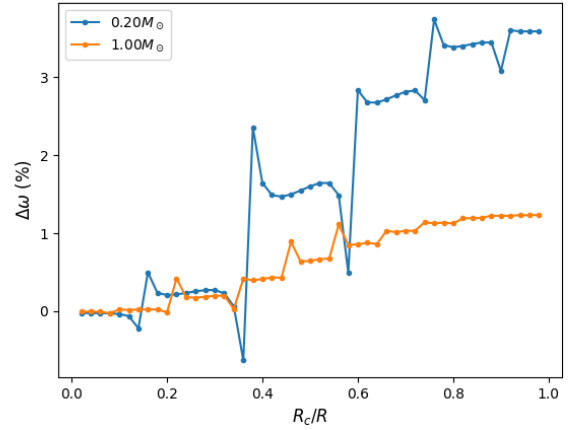


Figure 6. Percentage change of the f-mode frequency $\Delta\omega = (\omega - \omega_{\text{fluid}})/\omega_{\text{fluid}}$ due to the presence of a solid core is plotted against the (normalized) solid core radius R_c/R for two ^{16}O stars of different masses. The kinks are due to avoided crossings between the f-mode and other modes as illustrated in Figure 2.

core. However, the displacements are small in the fluid envelope. Its potential perturbation may continue oscillating in the fluid layer, and the oscillation depends on the frequency of the s-mode.

The general characteristics of the different modes discussed above remain the same when R_c/R increases. The eigenfunctions presented in Figures 3 to 5 are somewhat different from those in Fuller et al. (2014), where a fluid giant planet with a solid core is considered. They found that the f-mode is confined to the fluid layer while the s-modes are confined to the solid core. However, we show that the f-mode can have nonzero oscillations in the solid core, while the s_1 -mode oscillations can extend somewhat outside the core. The difference may be due to the fact that there is a density jump at the core-envelope interface in the giant planet model which does not exist in our models¹.

After examining the oscillation modes qualitatively, we investigate quantitatively how the mode frequencies change as the size of the crystallized core increases. Figure 6 plots the percentage change of the f-mode frequency $\Delta\omega = (\omega - \omega_{\text{fluid}})/\omega_{\text{fluid}}$ against the (normalized) core radius R_c/R for two ^{16}O stars of masses $0.20M_{\odot}$ and $1.00M_{\odot}$, where ω is the frequency for a crystallized WD model and ω_{fluid} is the frequency for the corresponding pure fluid counterpart. The spikes in the curves are due to avoided crossings between the f-mode and other modes (see Figure 2). The f-mode frequency generally increases with the solid core radius, and jumps in step at each avoided crossing, similar to Figure 2. In agreement with the estimation based on the μ/P ratio, the mode frequency indeed changes more significantly for the less massive star. For heavier stars, avoided crossing happens more frequently as the crystallized core grows, but the step sizes and spikes are smaller.

Similarly, Figure 7 compares the percentage change of the f-mode frequency for two $0.40M_{\odot}$ stars made of ^4He and ^{16}O respectively. Larger frequency changes are observed for stars of heavier elements as expected, since μ is proportional to $Z^{2/3}$. On the other hand,

¹ As a verification of our numerical code, we have also calculated the oscillation modes of the giant planet model in Fuller et al. (2014) and found that our results agree with those reported by them (see Appendix B).

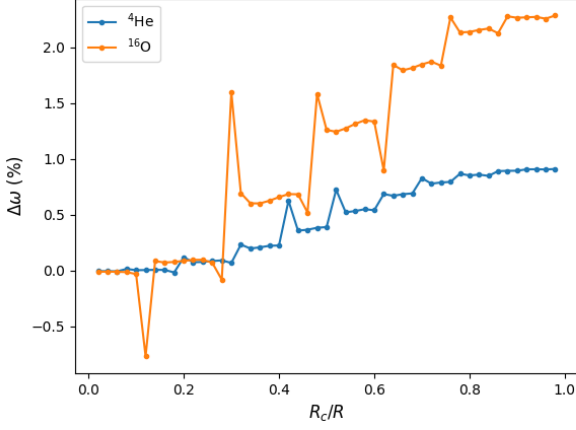


Figure 7. Similar to Figure 6, but for two $0.40M_{\odot}$ stars with different elements. The kinks are due to avoided crossings between the f-mode and other modes.

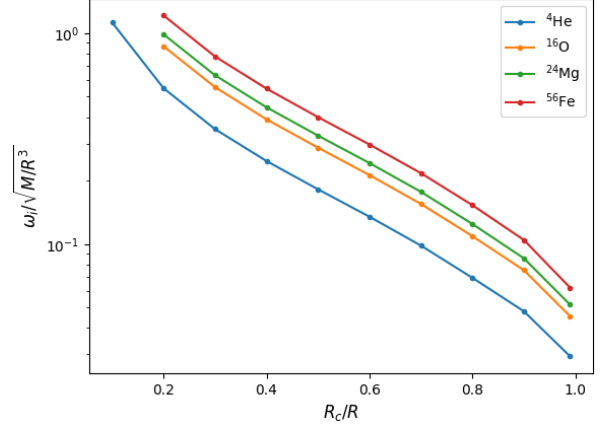


Figure 9. Similar to Figure 8, but for $0.40M_{\odot}$ stars of different elements.

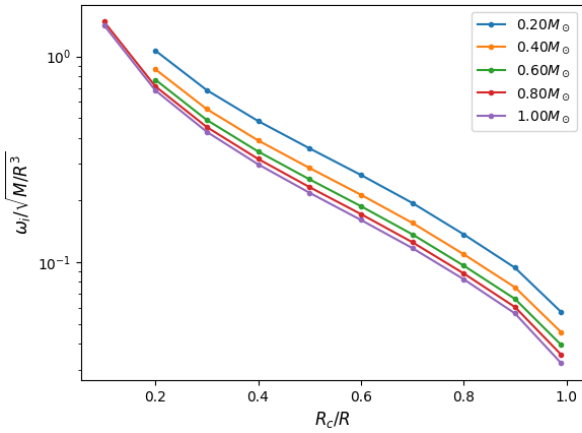


Figure 8. Comparison of the i-mode frequencies (normalized by $\sqrt{M/R^3}$) for ^{16}O stars of different masses.

more frequent avoided crossings with smaller step sizes and spikes are found for stars of lighter elements. In general, if a white dwarf is partially or fully crystallized, the f-mode frequency may deviate from its pure fluid value by a few percent.

In contrast, the i-mode frequency shows a simple decreasing trend as the solid core radius increases. Figure 8 plots the i-mode frequencies for ^{16}O stars of different masses against R_c/R . For better visualization of the data, we normalize the i-mode frequencies by the characteristic frequency $\sqrt{M/R^3}$ in the figure as the models have large differences in their masses and radii. It is seen that the i-mode frequency decreases as the core radius increases along a fixed mass sequence. The normalized i-mode frequency also decreases as the mass increases for a fixed value of R_c/R . Note, however, that the original (unnormalized) i-mode frequency actually increases with the mass. For instance, the i-mode frequency increases from 4.49 mHz to 23.7 mHz as the mass increases from $0.20M_{\odot}$ to $1.00M_{\odot}$ for $R_c/R = 0.6$. Four $0.40M_{\odot}$ stars of different elements are also compared in Figure 9, showing that the normalized i-mode frequency

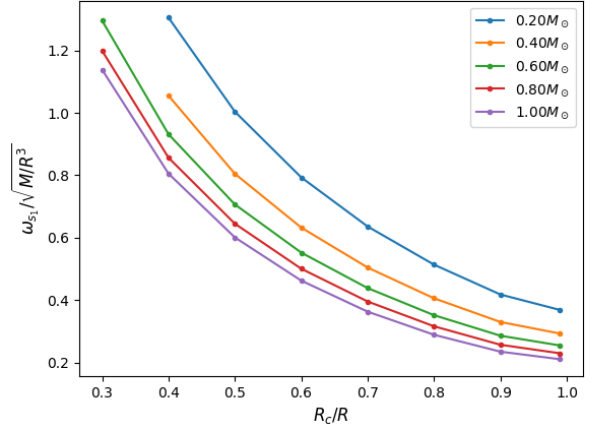


Figure 10. Comparison of the s_1 -mode frequencies (normalized by $\sqrt{M/R^3}$) for ^{16}O stars of different masses.

for lighter element is lower as well for a fixed value of R_c/R . In this case, the trends of the original and normalized i-mode frequencies are the same. Again, at $R_c/R = 1$, the i-mode does not exist and we only show the mode frequencies up to $R_c/R = 0.99$. If R_c/R increases further towards 1, the i-mode frequency drops rapidly to 0. Overall, the i-mode frequency can decrease to a few percent of $\sqrt{M/R^3}$ for $R_c/R \leq 0.99$.

For the s-mode, we show the frequencies of the s_1 -mode for ^{16}O stars of different masses and for $0.40M_{\odot}$ stars of different elements in Figures 10 and 11, respectively. The general trend is similar to that of the i-mode. The mode frequency decreases as the core radius increases for a fixed mass sequence. The mode frequency is also decreased for lighter elements.

In summary, the f-mode frequency increases with the solid core radius in steps due to the phenomenon of avoided mode crossings. The steps are larger for stars that are less massive or made of heavier elements, but are more frequent for stars that are massive or made of lighter elements. For the i-mode and s-mode, their frequencies decrease monotonically with the solid core radius.

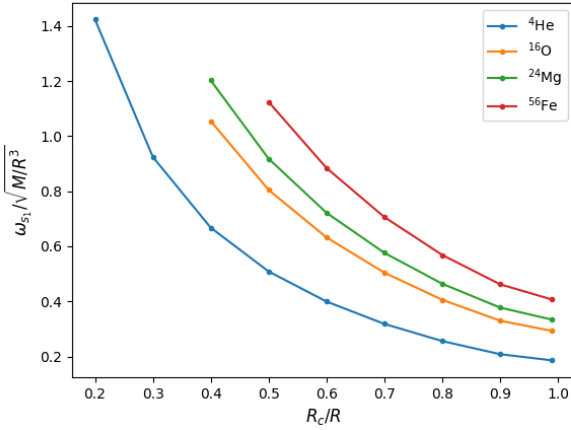


Figure 11. Similar to Figure 10, but for $0.40M_{\odot}$ stars of different elements.

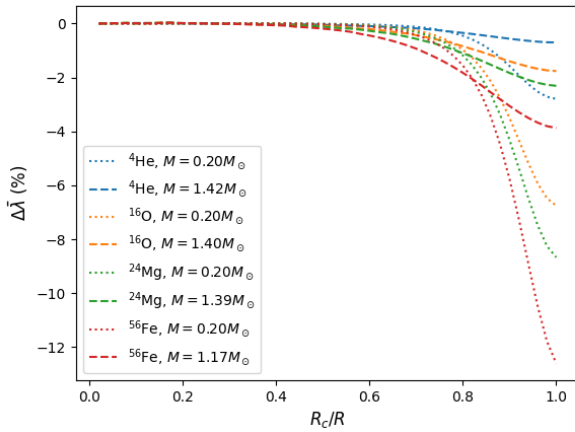


Figure 12. Percentage change of the scaled tidal deformability $\Delta\bar{\lambda} = (\bar{\lambda} - \bar{\lambda}_{\text{fluid}})/\bar{\lambda}_{\text{fluid}}$ as a function of the solid core radius, for different models near the maximum or minimum mass.

5.2 Tidal deformability

After studying the oscillation modes, we now turn our attention to the effect of crystallization on the tidal deformability. In Figure 12, we show how the scaled tidal deformability $\bar{\lambda} = \lambda/M^5$ deviates from its value in the pure fluid limit as the core radius increases. In the figure, the percentage change $\Delta\bar{\lambda} = (\bar{\lambda} - \bar{\lambda}_{\text{fluid}})/\bar{\lambda}_{\text{fluid}}$ is plotted against R_c/R for WD models with different masses and elements. For instance, the blue dotted line represents the results for a ${}^4\text{He}$ star with $0.20M_{\odot}$. It is seen that $\Delta\bar{\lambda}$ is very small when $R_c < 0.5R$ for all models. Its magnitude increases to only about 1% level even when the core radius increases to $R_c \approx 0.7R$. Hence, the fluid envelope can screen out the effect of the solid core significantly. This screening effect is present regardless of the element and mass of the models, though it is slightly weaker when the star is more massive. Such a screening effect due to the fluid envelope has also been seen in the study of the tidal deformability for hybrid star models featuring a crystalline color-superconducting quark-matter core (Lau et al. 2019). The change in $\bar{\lambda}$ becomes significant and depends sensitively on the star models

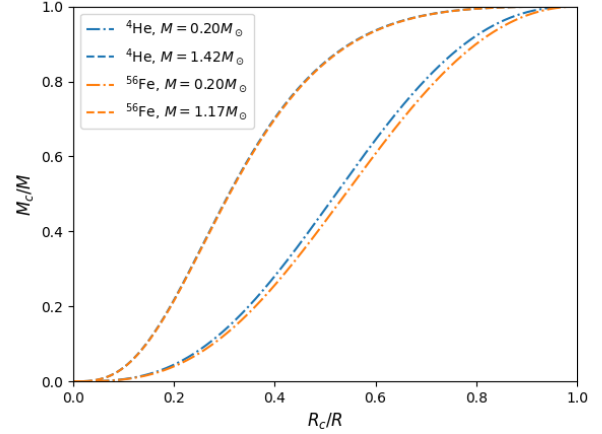


Figure 13. Relations between the crystallized mass fraction M_c/M and the normalized core radius R_c/R for ${}^4\text{He}$ and ${}^{56}\text{Fe}$ stars with different masses.

when $R_c \geq 0.7R$. For a given element, the deviation increases as the mass decreases. For a $0.20M_{\odot}$ ${}^{56}\text{Fe}$ star, the magnitude of $\Delta\bar{\lambda}$ can increase to more than 10% for a fully crystallized WD.

While we characterize the extent of crystallization by the (normalized) solid core radius R_c/R , observational studies often relate the effect by crystallized mass fraction M_c/M instead. To demonstrate the relation between the two quantities, we show M_c/M as a function of R_c/R for models of the heaviest (${}^{56}\text{Fe}$) and lightest (${}^4\text{He}$) elements in Figure 13. The curves for the two low-mass ($0.20M_{\odot}$) stars are close to each other. We also observe that more massive stars achieve higher M_c/M at lower R_c/R for both elements. In particular, the two high-mass cases $1.42M_{\odot}$ (${}^4\text{He}$) and $1.17M_{\odot}$ (${}^{56}\text{Fe}$) shown in the figure are stars near the Chandrasekhar limit of the corresponding elements. It is interesting to see that the two curves agree very well in this limit. We notice that the corresponding curves for all the WD models considered in this study basically lie in the region between the two orange lines in the figure.

5.3 Universal relations

Here we shall study the effects of crystallization on the I-Love and f-Love universal relations for WDs. While the I-Love-Q relations for pure fluid WD models have been studied in (Boshkayev et al. 2017; Boshkayev & Quevedo 2018; Taylor et al. 2020), we shall first use our own EOS models to verify the I-Love relation in the fluid limit. The moment of inertia I is simply calculated from the equilibrium fluid background, and hence is unaffected by the solid core. In Figure 14, we plot the scaled moment of inertia $\bar{I} \equiv I/M^3$ against $\bar{\lambda}$ for pure fluid WD models using our chosen EOS models discussed in Section 2, which include the Chandrasekhar model with the mean molecular weight per electron $\mu_e = 2$ (Chandrasekhar 1931, 1939), the BPS EOS (Baym et al. 1971), and the model described by equations (1)–(2) with different elements. We fit our numerical results using a 4th order polynomial fitting curve (solid line) of $\ln \bar{I}$ versus $\ln \bar{\lambda}$ which is given by

$$\ln \bar{I} = 0.710 + 0.233 \ln \bar{\lambda} + 0.00691 (\ln \bar{\lambda})^2 - 1.20 \times 10^{-4} (\ln \bar{\lambda})^3 + 7.51 \times 10^{-7} (\ln \bar{\lambda})^4. \quad (65)$$

The percentage deviation of the numerical data from the fitting curve is shown in the lower panel. It is seen that the I-Love relation is

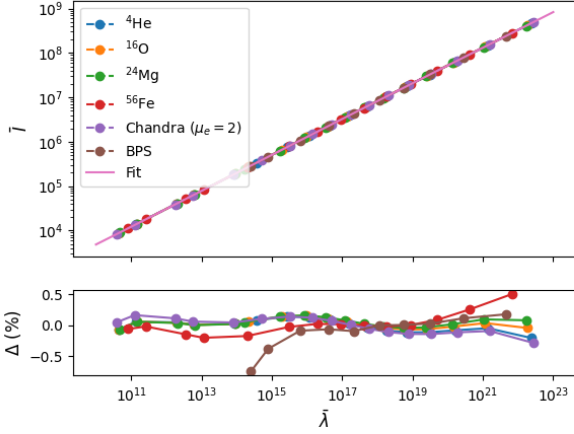


Figure 14. The I-Love relation for pure fluid WDs without solid cores. The numerical data are obtained from our chosen EOS models (see text for details). The solid line is the fitting curve given by equation (65). The percentage difference between the data and the fitting curve is shown in the lower panel. Note that the sequence for the BPS EOS is truncated close to the maximum-mass stable WD model where $\bar{\lambda} \approx 10^{14}$.

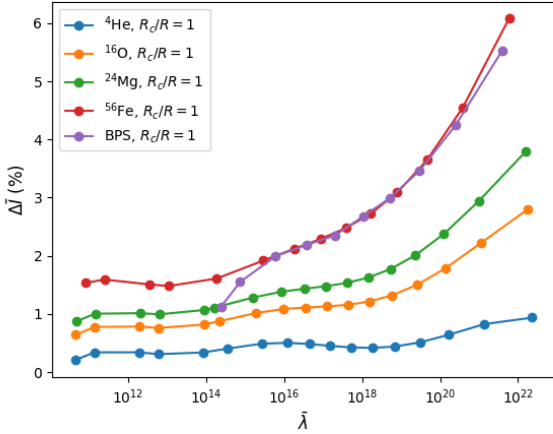


Figure 15. The percentage deviations of the scaled moment of inertia for crystallized WDs with solid core radius $R_c/R = 1$ from the prediction of the I-Love relation (equation (65)) for pure fluid WDs.

insensitive to the EOS models to within 1% level. The BPS model shows a larger deviation toward smaller values of $\bar{\lambda}$. Toward this end, the BPS model is reaching the maximum-mass instability limit. We note that the I-Love relation for pure fluid WDs has been provided before by Boshkayev & Quevedo (2018), but their data is truncated to 2 significant figures only. As the effect of crystallization on the I-Love relation is at most a few percent level (see below), we thus present a more accurate fitting curve for the I-Love relation in the fluid limit for the following investigation.

We now use the I-Love relation in the fluid limit (i.e., equation (65)) as a benchmark to compare with the results obtained by crystallized WD models. We define the percentage deviation $\Delta \bar{I} \equiv (\bar{I} - \bar{I}_{\text{Fit}}) / \bar{I}_{\text{Fit}}$, where \bar{I} is the moment of inertia of a crystallized WD and \bar{I}_{Fit} is the corresponding value predicted by equation (65) at the same

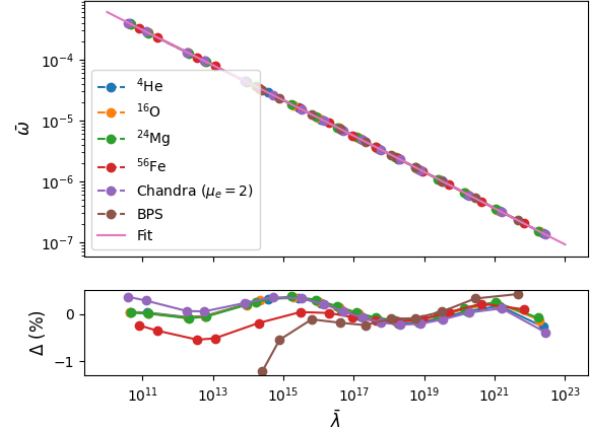


Figure 16. The f-Love relation for pure fluid WDs. The solid line is the fitting curve given by equation (66). The percentage difference between the data and the fitting curve is shown in the lower panel.

$\bar{\lambda}$. In Figure 15, we show $\Delta \bar{I}$ for fully crystallized WD models. It should be recalled that the moment of inertia is calculated from the fluid background star and is unchanged by crystallization. It is in fact the change in the tidal deformability due to the solid core for a given background model that produces the deviation. Note also that $\bar{\lambda}$ decreases with increasing stellar mass, and hence the region below $\bar{\lambda} \approx 10^{16}$ is occupied by WDs near the maximum mass limits. For these lower values of $\bar{\lambda}$, the percentage deviation $\Delta \bar{I}$ is below 2 percent. For higher values of $\bar{\lambda}$, corresponding to lower mass WDs, the deviation can be as large as about 5% for some models.

As a result, crystallization can break the I-Love relation of WDs, and the deviation is more significant for low mass WDs, though fully crystallized stars are needed to reach a deviation up to a few percent level.

After studying the effects of crystallization on the I-Love relation, we now turn to the f-Love relation which was originally discovered for neutron stars (Chan et al. 2014) and connects the scaled f-mode frequency $\bar{\omega} \equiv \omega M$ to $\bar{\lambda}$. As far as we are aware, the corresponding f-Love relation for pure fluid WDs has not been studied before and we shall fill this gap in the literature by establishing such a relation for WDs. In Figure 16, we plot $\bar{\omega}$ against $\bar{\lambda}$ for pure fluid WDs using our chosen EOS models. It is seen clearly that the results in fact lie on an approximate EOS-insensitive universal relation just like in the case of neutron stars. The solid line in the figure is a fitting curve given by

$$\ln \bar{\omega} = 1.66 - 0.570 \ln \bar{\lambda} + 0.0119 (\ln \bar{\lambda})^2 - 2.16 \times 10^{-4} (\ln \bar{\lambda})^3 + 1.40 \times 10^{-6} (\ln \bar{\lambda})^4. \quad (66)$$

The lower panel of Figure 16 shows the percentage deviation of the numerical data from the fitting curve and it is seen that the accuracy is within 1% level. Again, the BPS EOS shows a larger deviation when the stellar models approach the maximum-mass instability limit at smaller value of $\bar{\lambda}$.

However, similar to the I-Love relation, the f-Love relation is broken for crystallized WDs. As in the study of the breaking of the I-Love relation due to crystallization, we here define the percentage deviation $\Delta \bar{\omega} \equiv (\bar{\omega} - \bar{\omega}_{\text{Fit}}) / \bar{\omega}_{\text{Fit}}$, where $\bar{\omega}$ is the scaled f-mode frequency of a crystallized WD and $\bar{\omega}_{\text{Fit}}$ is the corresponding value predicted by equation (66) at the same $\bar{\lambda}$. In Figure 17, we plot $\Delta \bar{\omega}$

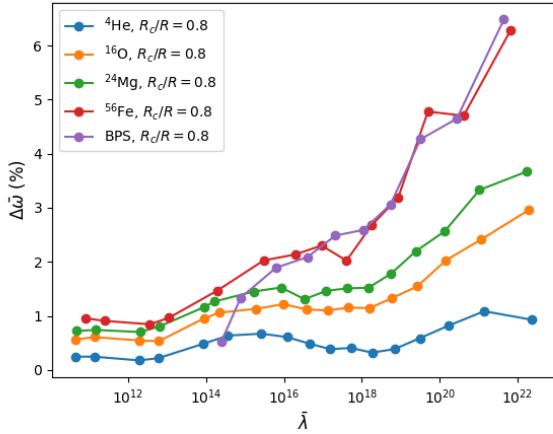


Figure 17. Percentage deviations from the f-Love relation (i.e., equation (66)) for stars with solid core radius $R_c/R = 0.8$. Similar to Figures 6 and 7, the kinks are due to the phenomenon of avoided mode crossings.

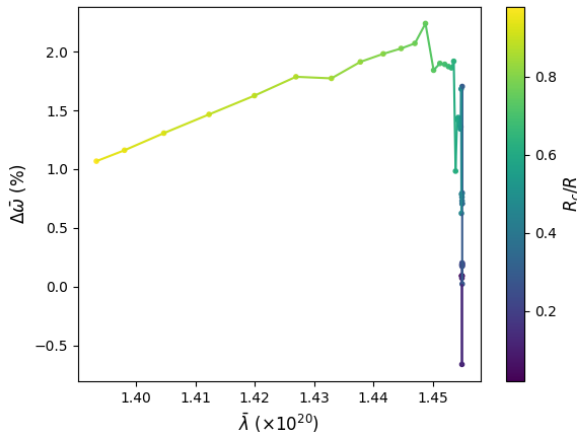


Figure 18. The trajectory of a $0.40M_\odot$ ^{16}O star in the $\Delta\bar{\omega} - \bar{\lambda}$ space. As the solid core radius R_c/R increases, its f-mode frequency increases and deviates from the f-Love relation. At higher R_c/R , $\bar{\lambda}$ quickly decreases, reducing the deviation from the f-Love relation. The kinks on the trajectory are due to the phenomenon of avoided mode crossings, and $\Delta\bar{\omega}$ does not start from 0 since the f-Love relation is only a fitting curve.

for crystallized WDs with solid core radius $R_c/R = 0.8$ against $\bar{\lambda}$ for our EOS models. As in the case of the I-Love relation, the effects of crystallization is small (within about 1% level) for smaller values of $\bar{\lambda}$, corresponding to the region near the maximum mass limits. The deviations become more significant as $\bar{\lambda}$ increases in the low-mass region. For instance, the percentage deviation for the BPS model with $0.2M_\odot$ reaches up to 6.5%. It is seen that there are kinks at various points along each sequence in Figure 17. They are due to the phenomenon of avoided mode crossings as discussed above. Similar to the breaking of I-Love relation, crystallization causes deviation from the f-Love relation by a few percent. The deviation is larger for star models composed of heavier elements or in the low-mass region with larger $\bar{\lambda}$.

If the core size grows beyond $0.8R$, one might guess that the

deviations would further increase. However, we found that this is not the case. In Figure 18, we demonstrate how a $0.40M_\odot$ ^{16}O star moves in the $\Delta\bar{\omega} - \bar{\lambda}$ plane as the core radius R_c/R grows from 0 to 1. It should be noted that the trajectory of the star does not start with $\Delta\bar{\omega} = 0$ when $R_c = 0$ since the f-Love relation is fit to the numerical data of different stellar models to about 1% only. When R_c/R is smaller than 0.5, the f-mode frequency increases and deviates from the f-Love relation, while $\bar{\lambda}$ remains unchanged due to the screening effect discussed in Section 5.2. The kinks at various points are due to the phenomenon of avoided mode crossings. But when R_c/R becomes larger, the deviation from the f-Love relation decreases. This is because $\bar{\lambda}$ starts decreasing rapidly as shown in Figure 12, moving the value closer to the f-Love relation.

6 CONCLUSIONS

The GW signals emitted from binary WD systems at the merger phase may be detectable by future space-borne GW detectors (Kinugawa et al. 2022). During the late inspiral when the WDs are close to each other, the tidal deformation and excitation of the f-mode oscillations of the WDs become important and contribute to the GW signals. The knowledge of the oscillation modes and tidal deformability of WDs is important to interpreting the observed GW signals. On the other hand, it is predicted that WDs in binaries may have evolved long enough to be fully or partially crystallized (van Horn 1968) and strong observational evidence has been found recently (Tremblay et al. 2019). It is thus important to study how crystallization inside WDs may affect the f-mode frequency and tidal deformability, and hence the emitted GW signals.

In this paper, we have studied not only the f-mode of WDs, but also the s- and i-modes which appear only when a crystalline core is present. For a given background WD model, we find that the frequencies of the s- and i-modes decrease as the radius of the core increases, while the f-mode frequency is affected only slightly. However, various avoided mode crossings occur when the frequencies of the f-mode and other modes approach each other as the core size increases. The f-mode frequency generally increases with the core radius and jumps in steps at the avoided crossing points. We also find that crystallization has a larger effect on the f-mode frequency for low mass WDs. For instance, the percentage change of the f-mode frequency for a fully crystallized ^{16}O WD (comparing to its pure fluid counterpart) increases from about 1% to 3% when the mass of the star decreases from $1.00M_\odot$ to $0.20M_\odot$.

The tidal deformability of crystallized WDs is also studied in this work. Due to a screening effect of the fluid envelope, the effect of the crystalline core in general becomes significant only when the core radius $R_c \geq 0.7R$. Similar to the case of f-mode, the effect increases as the mass decreases. For instance, the tidal deformability of a $0.2M_\odot$ ^{56}Fe fully crystallized WD can be different from that of a pure fluid counterpart by about 12%.

Similar to the situation for neutron stars, there exist approximate EOS-insensitive universal relations connecting the moment of inertia, tidal deformability, and f-mode frequency for pure fluid WDs. We have used our EOS models to verify the I-Love relation proposed by Boshkayev et al. (2017) and present a more accurate fitting curve for the study. We have also established the f-Love relation for fluid WDs for the first time. By taking the effects of elasticity in the calculations of the f-mode frequency and tidal deformability, we find that the universal relations can be broken for crystallized WDs. While the deviations are only about 1% level in the high-mass region near the maximum mass limits, the deviations for lower mass WDs

can be around 5 percent for some models. Therefore, crystallization may affect the results when universal relations are employed to infer the properties of WDs, such as the individual masses of the system, from the GW signals emitted from a WD binary (Wolz et al. 2021). On the other hand, the universal relations may be used to reduce the matter variables in theoretical waveform modellings for binary WDs. We may thus (in principle) infer the properties of crystallized WDs by comparing observation data against waveform models with and without the assumption of universal relations, though very accurate GW measurements would be needed.

However, as pointed out by Perot & Chamel (2022), fully ionized matter with completely degenerate electron gas at zero temperature is assumed in the EOS presented in Sec. 2. This approximation only holds in the crystallized core of WDs. Yet, for WDs that are cold enough to crystallize, we expect the deviation to be small in the fluid envelope as well. On the other hand, general relativistic effects are important for WDs near the maximum mass limit (Perot & Chamel 2022), thus the universal relations established by us in Newtonian gravity may be modified for high-mass WDs near this limit. These issues are left for a future investigation.

ACKNOWLEDGEMENTS

This work is partially supported by a grant from the Research Grant Council of the Hong Kong Special Administrative Region, China (Project No. 14300320).

DATA AVAILABILITY

The data underlying this article are available in the article. No new data needed to be generated or analyzed.

REFERENCES

- Alterman Z., Jarosch H., Pekeris C. L., 1959, *Proceedings of the Royal Society of London Series A*, 252, 80
- Althaus L. G., et al., 2021, *A&A*, 646, A30
- Amaro-Seoane P., et al., 2022, arXiv e-prints, p. arXiv:2203.06016
- Andersson N., Pnigouras P., 2019, arXiv e-prints, p. arXiv:1905.00012
- Baiko D. A., Potekhin A. Y., Yakovlev D. G., 2001, *Phys. Rev. E*, 64, 057402
- Barkett K., Chen Y., Scheel M. A., Varma V., 2020, *Phys. Rev. D*, 102, 024031
- Baym G., Pethick C., Sutherland P., 1971, *ApJ*, 170, 299
- Benvenuto O. G., De Vito M. A., 2005, *MNRAS*, 362, 891
- Boshkayev K., Quevedo H., 2018, *MNRAS*, 478, 1893
- Boshkayev K., Quevedo H., Zhami B., 2017, *MNRAS*, 464, 4349
- Breivik K., et al., 2020, *ApJ*, 898, 71
- Campos F., et al., 2016, *MNRAS*, 456, 3729
- Chamel N., Fantina A. F., 2016, *Phys. Rev. D*, 93, 063001
- Chan T. K., Sham Y. H., Leung P. T., Lin L. M., 2014, *Phys. Rev. D*, 90, 124023
- Chandrasekhar S., 1931, *ApJ*, 74, 81
- Chandrasekhar S., 1935, *MNRAS*, 95, 207
- Chandrasekhar S., 1939, *An introduction to the study of stellar structure*. University of Chicago Press
- Chugunov A. I., 2021, *MNRAS*, 500, L17
- Córsico A. H., 2020, *IAU Symposium*, 357, 93
- Córsico A. H., Althaus L. G., Montgomery M. H., García-Berro E., Isern J., 2005, *A&A*, 429, 277
- Cox J. P., 1980, *Theory of stellar pulsation*. Princeton University Press
- Crossley D. J., 1975, *Geophysical Journal*, 41, 153
- De Gerónimo F. C., Córsico A. H., Althaus L. G., Wachlin F. C., Camisassa M. E., 2019, *A&A*, 621, A100

- Fuller J., Lai D., 2011, *MNRAS*, 412, 1331
- Fuller J., Lai D., 2012, *MNRAS*, 421, 426
- Fuller J., Lai D., Storch N. L., 2014, *Icarus*, 231, 34
- García-Berro E., et al., 2010, *Nature*, 465, 194
- Gong Y., Luo J., Wang B., 2021, *Nature Astronomy*, 5, 881
- Isern J., Canal R., Labay J., 1991, *ApJ*, 372, L83
- Jordan George C. I., Perets H. B., Fisher R. T., van Rossum D. R., 2012, *ApJ*, 761, L23
- Kawamura S., et al., 2021, *Progress of Theoretical and Experimental Physics*, 2021, 05A105
- Kinugawa T., Takeda H., Tanikawa A., Yamaguchi H., 2022, *ApJ*, 938, 52
- Kobyakov D., Pethick C. J., 2015, *MNRAS*, 449, L110
- Korol V., Rossi E. M., Groot P. J., Nelemans G., Toonen S., Brown A. G. A., 2017, *MNRAS*, 470, 1894
- Lackey B. D., Pürrer M., Taracchini A., Marsat S., 2019, *Phys. Rev. D*, 100, 024002
- Lamberts A., Blunt S., Littenberg T. B., Garrison-Kimmel S., Kupfer T., Sanderson R. E., 2019, *MNRAS*, 490, 5888
- Lau S. Y., Leung P. T., Lin L.-M., 2019, *Phys. Rev. D*, 99, 023018
- Li Z., Chen X., Chen H.-L., Li J., Yu S., Han Z., 2020, *ApJ*, 893, 2
- Liebert J., Bergeron P., Eisenstein D., Harris H. C., Kleinman S. J., Nitta A., Krzesinski J., 2004, *ApJ*, 606, L147
- Montgomery M. H., Winget D. E., 1999, *ApJ*, 526, 976
- Nelemans G., Tauris T. M., 1998, *A&A*, 335, L85
- Nelemans G., Yungelson L. R., Portegies Zwart S. F., Verbunt F., 2001, *A&A*, 365, 491
- Nomoto K., 1984, *ApJ*, 277, 791
- Perot L., Chamel N., 2022, *Phys. Rev. D*, 106, 023012
- Poisson E., Will M. W., 2014, *Gravity: Newtonian, Post-Newtonian, Relativistic*. Cambridge University Press
- Rathore Y., Blandford R. D., Broderick A. E., 2005, *MNRAS*, 357, 834
- Ruan W.-H., Liu C., Guo Z.-K., Wu Y.-L., Cai R.-G., 2020, *Nature Astronomy*, 4, 108
- Saumon D., Blouin S., Tremblay P.-E., 2022, *Phys. Rep.*, 988, 1
- Schmidt P., Hinderer T., 2019, *Phys. Rev. D*, 100, 021501
- Taylor A. J., Yagi K., Arras P. L., 2020, *MNRAS*, 492, 978
- Tremblay P.-E., et al., 2019, *Nature*, 565, 202
- Winget D. E., Kepler S. O., Campos F., Montgomery M. H., Girardi L., Bergeron P., Williams K., 2009, *ApJ*, 693, L6
- Wolz A., Yagi K., Anderson N., Taylor A. J., 2021, *MNRAS*, 500, L52
- Yagi K., 2014, *Phys. Rev. D*, 89, 043011
- Yagi K., Yunes N., 2013a, *Phys. Rev. D*, 88, 023009
- Yagi K., Yunes N., 2013b, *Science*, 341, 365
- van Horn H. M., 1968, *ApJ*, 151, 227

APPENDIX A: BOUNDARY CONDITIONS AT THE CENTER

Near the center, the y 's can be expanded using coefficients presented in Crossley (1975), and the derivatives can be obtained by plugging the expansions into equations (25) to (30). However, severe numerical cancellation occurs among y_2' , y_4' , and y_6' when $l \geq 1$. To fix this issue, we evaluate the expansion of their derivatives near the center according to

$$y_2' = 2\mu l(l-1)(l-2)Cr^{l-3} + (-\rho\omega^2 - 4\rho\gamma)Ar^{l-1} \\ + l(l+1)\rho\gamma Cr^{l-1} - \rho Fr^{l-1} + 2\delta A'r^{l-1} - 4\mu\beta B'r^{l-1} \\ - l(l+1)\delta C'r^{l-1} + l(l+1)D'r^{l-1} \quad (A1)$$

$$y_4' = 2\mu(l-2)(l-1)Cr^{l-3} + lD'r^{l-1} + \rho\gamma A'r^{l+1} - \rho\omega^2 C'r^{l+1} \\ - \rho E'r^{l+1} \quad (A2)$$

$$y_6' = (l-1)Fr^{l-2} - 3\gamma l(l+1)C'r^l + l(l+1)E'r^l - 2F'r^l, \quad (A3)$$

Table B1. Comparison between f-mode, s_1 -mode and i-mode frequency of the Saturn model in Fuller et al. (2014) computed by our code and computed by Fuller et al. (2014).

Mode	$\sqrt{\omega^2 R^3 / M}$ (Our work)	$\sqrt{\omega^2 R^3 / M}$ (Fuller)
f	1.316	1.312
s_1	0.411	0.413
i	2.773	2.770

where the coefficients A , B , C , etc, are given by equations (42) to (50). For y'_1 , y'_3 , and y'_5 , equations (25), (27) and (29) can be applied directly.

When r is small, we integrate the y 's using the above expansions. But when r is larger such that the numerical cancellation is under control, we switch back to equations (25) to (30).

APPENDIX B: CODE TESTS

The calculation of oscillation modes is divided into the crystalline core and fluid envelope. We have checked that our code can reproduce the f-mode frequency of a $n = 1$ polytropic star (i.e. $P \propto \rho^2$) in the pure fluid limit (see Table 17.2b of Cox 1980) to within 0.1% accuracy when either the core radius is set to be very small (e.g., $R/R_c = 0.01$) or the shear modulus of a finite-size core is set to be much smaller than the central pressure.

To further validate our oscillation code, we test it using the Saturn model in Fuller et al. (2014), which is constructed from a $n = 1$ polytropic model by multiplying a factor of 4 to the density in the core ($r < 0.25R$), and normalizing the density profile such that the mass and radius equal to those of Saturn. In contrast to our white dwarf models, there is a density jump at the core-envelope interface in their Saturn model which we have also taken into account in the test. Since Fuller et al. (2014) did not report a precise value of the radius of their model, we chose a model that best matches their density, bulk modulus and gravity profiles. We have checked that our code accurately reproduces the f-mode, s_1 -mode, and i-mode frequencies as presented in Table B1. Note that the numerical results of Fuller et al. (2014) are extracted from their figures.

This paper has been typeset from a $\text{\TeX}/\text{\LaTeX}$ file prepared by the author.